

## Article

# Biogeochemical Permeable Barrier Based on Zeolite and Expanded Clay for Immobilization of Metals in Groundwater

Nadezhda Popova <sup>1</sup>, Grigoriy Artemiev <sup>1</sup>, Inga Zinicovscaia <sup>2,3,4</sup>, Nikita Yushin <sup>2</sup>, Ludmila Demina <sup>1</sup>, Kirill Boldyrev <sup>5</sup> and Alexey Safonov <sup>1,\*</sup>

<sup>1</sup> A.N. Frumkin Institute of Physical Chemistry and Electrochemistry, Russian Academy of Sciences, 31-4, Leninsky Prospect, 199071 Moscow, Russia

<sup>2</sup> Joint Institute for Nuclear Research, 6 Joliot-Curie Str., 141980 Dubna, Russia

<sup>3</sup> Horia Hulubei National Institute for R&D in Physics and Nuclear Engineering, 30 Reactorului Str. MG-6, 077125 Magurele, Romania

<sup>4</sup> The Institute of Chemistry, 3 Academiei Str., 2028 Chisinau, Moldova

<sup>5</sup> The Nuclear Safety Institute of the Russian Academy of Sciences 52, Bolshaya Tuskaya Street, 115191 Moscow, Russia

\* Correspondence: alexeysafonov@gmail.com

**Abstract:** Groundwater samples contaminated with potentially toxic elements (PTE), including metals and nitrate ions, were collected at a depth of 8–10 m from the Siberian Chemical Plant multicomponent waste storage. The possibility of developing a permeable biogeochemical barrier with zeolite and lightweight expanded clay aggregate (LECA) was investigated. The mass fraction and properties of several metals (Mn, Fe, Co, Ni, Cu, Zn, Cd, Hg and Pb) were determined to investigate their fixation on the chosen materials at the given experimental conditions. It was established that metals in sulfide or phosphate forms can be effectively immobilized via biomineralization on LECA, whereas metals from the non-chalcogen group are primarily retained in the form of phosphates. The formation of biogenic deposits of iron sulfide, which serve as a sorption–precipitation phase during the immobilization of the majority of metals, is an important aspect of the LECA loading process. The use of LECA and zeolite in the form of a two-component barrier is feasible based on the data obtained. It is assumed that metal immobilization processes occur due to sorption mechanisms in the zone of zeolite loading. Microbial nitrate removal and the formation of iron sulfide phases under reducing conditions, which form a geochemical barrier for metals, are expected in the LECA zone.

**Keywords:** mesoporous zeolite; lightweight expanded clay aggregate (LECA); aquifer contamination; permeable barrier; potentially toxic elements (PTE); sorption; biomineralization



**Citation:** Popova, N.; Artemiev, G.; Zinicovscaia, I.; Yushin, N.; Demina, L.; Boldyrev, K.; Sobolev, D.; Safonov, A. Biogeochemical Permeable Barrier Based on Zeolite and Expanded Clay for Immobilization of Metals in Groundwater. *Hydrology* **2023**, *10*, 4. <https://doi.org/10.3390/hydrology10010004>

Academic Editor: Meysam Vadiati

Received: 7 December 2022

Revised: 15 December 2022

Accepted: 17 December 2022

Published: 24 December 2022



**Copyright:** © 2022 by the authors. Licensee MDPI, Basel, Switzerland. This article is an open access article distributed under the terms and conditions of the Creative Commons Attribution (CC BY) license (<https://creativecommons.org/licenses/by/4.0/>).

## 1. Introduction

Electroplating enterprises, solid waste landfills, as well as mining activities, ore processing, chemical and metalworking industries contribute to the contamination of both underground and surface waters with potentially toxic elements (PTE: heavy metals and acid anions). The most pronounced detrimental effect on the environment can be caused by industrial effluents stored in the form of dumps or sludge, and in surface storage pools [1–3]. Notwithstanding the fact that many techniques for remediation of contaminated soils and surface water bodies have been created and are continuously improved, the treatment of contaminated groundwater continues to be an expensive and difficult task.

Various impermeable (e.g., cut-off walls in the ground) or permeable engineering barriers have traditionally been used to prevent pollutant migration in groundwater [4]. Permeable barriers are considered to be a better long-term solution, as they do not disrupt groundwater movement and do not induce blockages in the geologic horizon [5–7]. A variety of natural materials, including zeolites [8–10], limestone [6,11], apatite [12], artificially created materials such as cement-based filter media (CBFM) [13], waste products (e.g., fly

ash [14]), as well as numerous organic materials and their compositions with minerals [15], can be used to create these barriers. The formation of in situ geochemical barriers using reducing agents, such as zero-valent iron [16,17] and other additives, is another method of treating groundwater. Their injection into the groundwater formation creates local zones for metal immobilization.

One of the promising remediation strategies for combating multicomponent contamination is the application of in situ biogeochemical barriers based on sorbents and highly porous material, as well as microorganism growth stimulation by organic compounds. Numerous studies have employed this strategy [18,19]. The development of microbial biofilms that protect microorganisms from the toxic effects of the contaminated environment and allow the microbial community to effectively cope with it is critical for the successful operation of such barriers [20]. Shortcomings of this approach include the necessity of extra nutrition for the microorganisms as well as biofouling of highly effective sorptive materials causing deterioration of their properties. Biofilms, on the other hand, can improve material sorption capacity since their polysaccharide matrix contains a significant number of functional groups, which can participate in metal sorption [21–24]. Furthermore, microbial processes can result in the formation of secondary mineral phases, such as sulfide or ferruginous phases, which additionally contribute to metal immobilization [25–27].

Previously, we have studied the possibility of using zeolite, apatite, expanded clay, vermiculite, and other materials along with organic stimulation as a groundwater permeable barrier near a storage facility for the immobilization of radionuclides, such as cesium, strontium, uranium, and technetium, from radioactive waste [28]. The effects of natural groundwater microflora on the sorption properties of materials were studied. It was demonstrated that microbiological effects did not significantly alter the sorption properties of the examined materials under the operating conditions of the barrier. In another study, the possibility of using vermiculite, lightweight expanded clay aggregate (LECA), perlite, zeolite, and shungite as filtration barrier in the aquifer near a solid domestic waste landfill for Cd and Cr (VI) immobilization was investigated. Based on the results obtained by authors of the present study and other researchers [4], the most optimal approach in case of purification of groundwater with multi-component contamination is development of permeable barriers consisting of several materials that create different conditions for the immobilization of various contaminants.

The aim of the present study was to assess the possibility of using zeolite and LECA as a permeable biogeochemical engineering barrier in groundwater with high nitrate and sulfate contamination for metal ion immobilization, taking as an example, groundwater collected near the multicomponent waste storage of the Siberian Chemical Plant (Tomsk region, Russia).

A field test to create a groundwater biogeochemical barrier was conducted there previously [29]. In less than one month, as a result of a single injection of organic matter, the studied area was cleared of nitrate ions, but the effect was transient; in one year, concentrations of contaminants comparable to the initial ones were observed in the stonecrop zone. In this case, enhancing the stable development of microorganisms in biofilms in contaminated groundwater could be a critical solution for in situ nitrate, radionuclide, and various metal removals.

## 2. Materials and Methods

In the present study, a groundwater sample was collected from a depth of 8–10 m in the area of the basin of the Siberian Chemical Plant storage of polycomponent wastes. Water samples were taken after pumping one and a half well volumes in sterile, 2 L plastic bottles, hermetically sealed and stored at a temperature of +4 °C in a refrigerator. The sample chemical composition and microbiological properties can be found in [29]. It contained high concentrations of major components, nitrate ions and calcium, as well as PTE—Mn, Fe, Ni, Cu, Sr, and Zn (Table 1).

**Table 1.** Characteristics of the analyzed groundwater sample.

Major Elements *, mg/L		Trace Elements **, µg/L					
pH	6.34 ± 0.2	Al	145 ± 4.4	As	0.6 ± 0.1	Cs	0.01 ± 0.001
salt concentration	6670 ± 200	Si	9893 ± 297	Br	128 ± 0.2	Ba	612 ± 18.4
Na <sup>+</sup>	647 ± 19	Sc	2 ± 0.1	Se	2.7 ± 0.1	La	0.74 ± 0.02
K <sup>+</sup>	8.9 ± 0.3	Ti	3.1 ± 0.1	Rb	0.25 ± 0.2	Ce	1.16 ± 0.04
Ca <sup>2+</sup>	762.3 ± 22.8	V	0.9 ± 0.02	Sr	993 ± 30	W	0.3 ± 0.01
Mg <sup>2+</sup>	139.7 ± 4.2	Cr	5.06 ± 0.2	Zr	0.1 ± 0.01	Pb	0.92 ± 0.03
NH <sub>4</sub> <sup>+</sup>	12.3 ± 0.03	Mn	4482 ± 135	Nb	0.3 ± 0.01	Th	0.04 ± 0.001
NO <sub>3</sub> <sup>-</sup>	3849 ± 115	Fe	17563 ± 527	Mo	2.24 ± 0.06	U	0.72 ± 0.02
SO <sub>4</sub> <sup>2-</sup>	467 ± 14	Co	16.5 ± 0.5	Ru	0.03 ± 0.001		
Cl <sup>-</sup>	6.3 ± 0.2	Ni	145 ± 4.4	Rh	2.03 ± 0.06		
HCO <sub>3</sub> <sup>-</sup>	305.1 ± 9.2	Cu	60 ± 1.8	Pd	0.02 ± 0.001		
P <sub>tot</sub>	32.5 ± 1	Zn	150 ± 4.5	Cd	11.3 ± 0.34		

\* Detection limit = 100 µg/L, with the exceptions of K, Cl = 10 µg/L, and P = 25 µg/L. \*\* Detection limit: As, Nb, Ba = 0.1 µg/L; Br = 16 µg/L; Se = 1.6 µg/L; Zr, Nb, Ru, Pd, Cd, W = 0.01 µg/L; Mo, Pb = 0.02 µg/L; Cs = 0.001 µg/L; La = 0.003 µg/L; Ce = 0.004 µg/L; Th, U = 0.002 µg/L.

### 2.1. Carriers

Natural zeolite (Clinoptilolite type) from the Chola deposit (Transbaikalia, Russia) was purchased from the “Zeolite-Trade” company (<http://www.zeolite.spb.ru/> accessed on 17 January 2021). The zeolite “Trade” consists of isometric aggregates of 3–5 mm and microaggregates of micron size with thin isometric pores and elongate channels. This structure ensures simultaneous high filtration and sorption properties. The density of the “Trade” zeolite is 2.2–2.6 g/cm<sup>3</sup>, the specific surface area is 10.1 m<sup>2</sup>/g, and the bulk weight is 1.02–1.2 g/cm. Natural zeolite was ground up and sieved, and the fraction with a size 300–100 µm was used for further experiments.

Lightweight expanded clay aggregate (LECA) produced by the PJSC “Keramzit” (Serpukhov, Russia, <https://zao-keramzit.com>) (accessed on 26 January 2021). Is a mixture of clay minerals (smectite, beydelite) heated at 1200 °C. It is composed of highly porous aggregates up to 5 mm in size and pores ranging from several nanometers to 0.5 mm. Despite its high porosity and specific surface, the LECA has a low chemical activity due to the highest and most stable oxidation state of its components during burning, when water and organic matter are completely removed.

### 2.2. Experimental Design

#### 2.2.1. Sorption before and after Biofouling

In the first stage, the experiments were performed on materials with biofilm formed by the groundwater microbial community. The biofouling was performed in aerobic conditions for 14 days in Adkins media inoculated with 10% of groundwater sample. The medium contained NH<sub>4</sub>Cl—1.0; KH<sub>2</sub>PO<sub>4</sub>—0.75; K<sub>2</sub>HPO<sub>4</sub>—1.5; NaNO<sub>3</sub>—1.0; NaCl—0.8; Na<sub>2</sub>SO<sub>4</sub>—0.1; MgSO<sub>4</sub>·7H<sub>2</sub>O—0.1; KCl—0.1, yeast extract—0.5; glucose—1.0; CH<sub>3</sub>COONa—1.0, pH = 7. Glucose and sodium acetate Sigma Aldrich (Darmstadt, Germany) (<https://www.sigmaaldrich.com/> accessed on 1 March 2021.) in concentrations of 1 g/L were used as carbon sources and electron donors. Filtration and freeze drying were used to separate the biofilm-containing materials from the cultivation medium.

Sorption experiments were conducted in 100 mL flasks for 24 h at vigorous agitation with the same groundwater. The solution volume was 50 mL, and the sorbent dosage was 0.5 g. Metals were added from nitrate solutions (Sigma Aldrich (Darmstadt, Germany)) at a concentration of 10 mg /L (per metal). All experiments were conducted in triplicate, and the average values were used for further calculations.

The metal uptake  $q$  (mg/g sorbent) was calculated using the following equation:

$$q = \frac{V(C_i - C_f)}{m} \quad (1)$$

and sorption removal efficiency,  $R$  (%), from the equation:

$$R = \frac{C_i - C_f}{C_i} * 100 \quad (2)$$

where  $q$  is the amount of metal ions adsorbed on the sorbent in mg/g;  $V$  is the volume of solution in ml;  $C_i$  is the initial concentration of a metal in mg/L,  $C_f$  is the final metal concentration in the solution in mg/L, and  $m$  is the mass of sorbent in g.

Desorption was carried out with low mineralized model water (NaHCO<sub>3</sub>—25.2, MgSO<sub>4</sub>·7H<sub>2</sub>O—36.6, CaCl<sub>2</sub>·6H<sub>2</sub>O—223.9, MgCO<sub>3</sub>—3.2, NaNO<sub>3</sub>—1000, pH 7.1) In vials, the material was stirred at 120 rpm for 2 h at room temperature. All chemicals were high purity grade from Sigma Aldrich (Darmstadt, Germany).

### 2.2.2. Metal Immobilization during Microbial Growth

In the second stage, an experiment on accumulation and biomineralization of mineral carriers with simultaneous growth of microorganisms from the solution of underground water was carried out. Sodium acetate and glucose high purity grade (Sigma Aldrich, Darmstadt, Germany) at a concentration of 1 g/L were used as a carbon source and electron donors. The experiment was carried out in hermetically sealed vials for one month to achieve anaerobic mineralization of iron and sulfur. Metals at the same concentrations as in the sorption experiment were added to the medium in the beginning of the experiment.

The medium in the first stage of the experiment contained phosphates from groundwater samples; in the second variant, phosphates at a concentration of 500 mg/L in the form of potassium phosphate high purity grade (Sigma Aldrich, Darmstadt, Germany) were added. Desorption was carried out according to the procedure described for sorption experiment.

### 2.3. Methods

The chemical composition of the water samples was analyzed immediately after sample collection and filtration through a 0.45 μm glass filter by inductively coupled plasma–mass spectrometry (ICP-MS) on mass spectrometer Xseries II ICP-MS (Thermo Fisher Scientific, Waltham, MA, USA) and ICP-OES on ICP-OES CID Spectrometer); iCAP 6500 (Thermo Fisher Scientific, Waltham, MA, USA, <https://www.fishersci.com/shop/products/icap-6500duoview-icp-oes-spect/NC1982295> accessed on 19 January 2022).

The determination of Eh and pH values was carried out using an ANION-4100 pH meter/ionomer (Russia) with an electrode combination. Anion and cation concentrations were measured by a CGE capillary electrophoresis system (Capel-105M, LUMEX Instruments, Saint Peterburg, Russia, <https://www.lumexinstruments.com/catalog/capillary-electrophoresis/capel-105m.php> accessed on 10 January 2020).

Copper, Cd, and Pb concentrations in the solutions were determined by AAS (Thermo Scientific iCE 3400 series, Waltham, MA, USA, <https://www.thermofisher.com/order/catalog/product/942350023411>) (accessed on 6 December 2022) with electrothermal atomization. Calibration solutions were prepared from a 1 g/L stock solution (AAS standard solution; Merck, Darmstadt, Germany).

The mass fraction of other elements was determined using neutron activation analysis at the pulsed fast reactor IBR-2 (Frank Laboratory of Neutron Physics, Joint Institute for Nuclear Research, Dubna, Russia). The concentration of Mn was determined by irradiation for 3 min at a thermal neutron flux of  $1.2 \times 10^{12}$  n cm<sup>-2</sup> s<sup>-1</sup>, and measurement time was 15 min. To determine the mass fraction of elements with long-lived isotopes: Cr, Co, Zn, Sr, Ba, and Hg samples were irradiated for 4 days at a neutron flux of  $1.1 \times 10^{11}$  cm<sup>-2</sup> s<sup>-1</sup>. Gamma spectra of induced activity were obtained after 4 and 20 days using three Canberra HPGe detectors with an efficiency of 40–55% and resolution of 1.8–2.0 keV at 1332 keV <sup>60</sup>Co total-absorption peak. The analysis of the spectra was performed using the Genie2000 software by Canberra (<https://www.mirion.com/products/genie-2000-basic-spectroscopy-software>) (accessed on 6 December 2022), with peak fitting verification in interactive mode.

The calculation of the concentrations was carried out using the software “Concentration” developed in FLNP [30].

Biofilm development was detected using confocal scanning microscopy. The samples were washed with distillate water to remove planktonic cells prior to storing in a 96% alcohol solution for biofilm fixation. ConA (lectin conjugated with the fluorescent dye Alexa Fluor 488 (C11252, ThermoFisher) in phosphate buffer at a dilution of 1:500) and SYBR Green II (S7564, ThermoFisher), which binds to nucleic acids (primarily RNA), were used to stain the samples. ConA binds to bacterial wall monosaccharides and EPS, SYBR Green II to nucleic acid. Staining was performed in the dark for 30 min on a shaker at room temperature. The samples were analyzed using a Zeiss LSM880 confocal microscope (Zeiss, Germany). The images were acquired with x20 and x40 objectives and argon lasers with wavelengths of 488 nm for detecting ConA fluorescence and 543 nm for detecting SYBR Green II. The Nomarski contrast method was applied to detect uncolored particles (LECA and zeolite). The obtained images were analyzed using the ImageJ software package with the plugin BioFormats 5.8.2 (<https://docs.openmicroscopy.org/bio-formats/5.8.2/about/index.html>) (accessed on 6 December 2022) and BioFilmAnalyzer v.1.0 [31].

Organic carbon was determined using a total organic carbon analyzer: Shimadzu TOC-V CSN (Kyoto, Japan).

Respiration activity was determined using the MTT test under oxic and anoxic conditions [32]. Before spectrophotometry of the oxidized formazan complex, the samples were centrifuged at 7000 g to remove the clay suspension.

Materials surface analysis before and after sorption was performed using a S3400N scanning electron microscope (Hitachi, Santa Clara, CA, USA). Analysis samples were removed from the liquid medium by filtration and dried at room temperature in a nitrogen glove box to a constant weight. For SEM analysis, the samples were placed on an aluminum holder using electrically conductive tape, and vacuum carbon deposition (Q150T E Plus) was carried out (vacuum 4–3, current 50 A). The samples were analyzed in two modes, SE and BSE, at a voltage of 20 kV.

Fourier-transform infrared (FT-IR) spectroscopy was used to confirm the presence of the functional groups in the microbial samples. Infrared spectra were recorded in the 4000–550  $\text{cm}^{-1}$  region using a Thermo Nicolet Nexus 4700 FT-IR Spectrometer (Thermo Fisher Scientific, Waltham, MA, USA).

The speciation of metals in solution was assessed by thermodynamic modeling in the Phreeqc 2.1 software with the llnl.dat thermodynamic database [33]. The saturation indices (SI) were determined as follows:

$$SI = \log IAP - \log K_s \quad (3)$$

where  $IAP$  is the product of activities of the relevant ions, and  $K_s$  is the equilibrium constant. At  $SI > 0$ , formation of the studied phase is predicted.

### 3. Results

#### 3.1. Zeolite and LECA Biofilm Characterization

The microbial biofilm formation and the accumulation of organic carbon on the materials occurred after a single stimulation with glucose. Organic carbon is predominantly present as the biofilm exopolysaccharide matrix. The maximum carbon accumulation on zeolite was observed on days 20–30, and on LECA on days 15–20 (Table 2). LECA had a higher total carbon mass fraction, reaching 12.9 mg/g. A gradual biofilm degradation on both materials was observed after 40 days. After 60 days, the carbon mass fraction on zeolite decreased to the initial values of biofilm development; for LECA, the decrease was 15% from the maximum.

**Table 2.** Kinetics of total organic carbon accumulation on the studied materials (mg/g) \*.

Sample	Time, Days								
	0	5	7	15	20	30	40	50	60
Zeolite	0.12 ± 0.004	3.8 ± 0.13	4.6 ± 0.15	7.1 ± 0.22	8.5 ± 0.3	8.4 ± 0.3	4.5 ± 0.15	3.9 ± 0.13	3.5 ± 0.11
LECA	0.26 ± 0.01	4.5 ± 0.15	7.9 ± 0.3	12.8 ± 0.45	12.9 ± 0.4	12.4 ± 0.43	11.5 ± 0.38	11.0 ± 0.35	10.9 ± 0.33

\* Uncertainty of the TOC result is less than 5%, according to the Shimadzu TOC Measurement Manual.

The morphology of the samples was visualized using confocal laser scanning microscopy (Figure 1). It was discovered that the LECA coverage by biofilm was more even than biofouling on zeolite. On the 20th day, the total area of polysaccharides on LECA was  $75 \pm 3.8\%$ , taking into account that the total area of fouling was  $89 \pm 4.3\%$ . The area covered by polysaccharides on zeolite was  $54 \pm 2.6\%$ , the total fouling area being  $59 \pm 2.9\%$ .

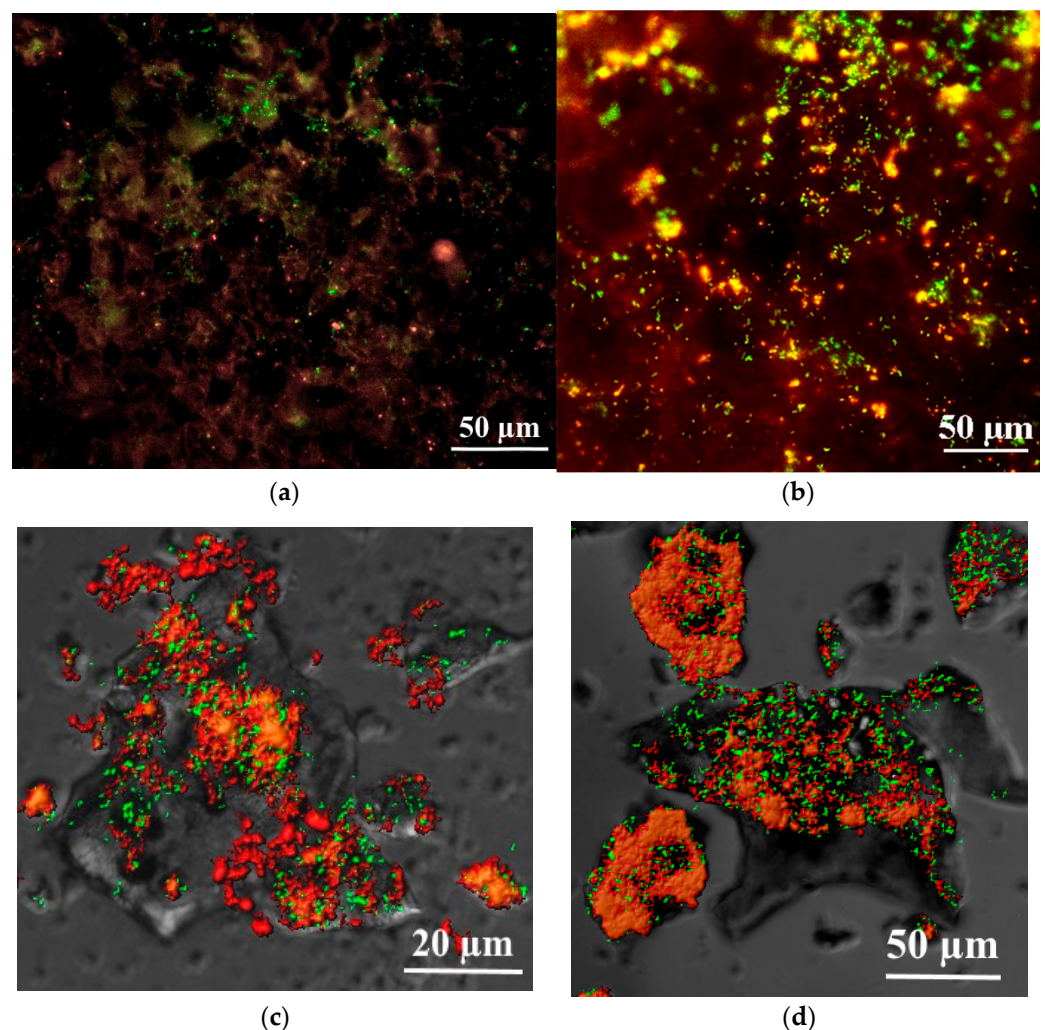


**Figure 1.** Micrographs of materials on the 20th day: zeolite–bio (a), zeolite–biomineralization (b), LECA–bio (c) and LECA–biomineralization (d). Red channel is polysaccharides, and green is nucleic acids.

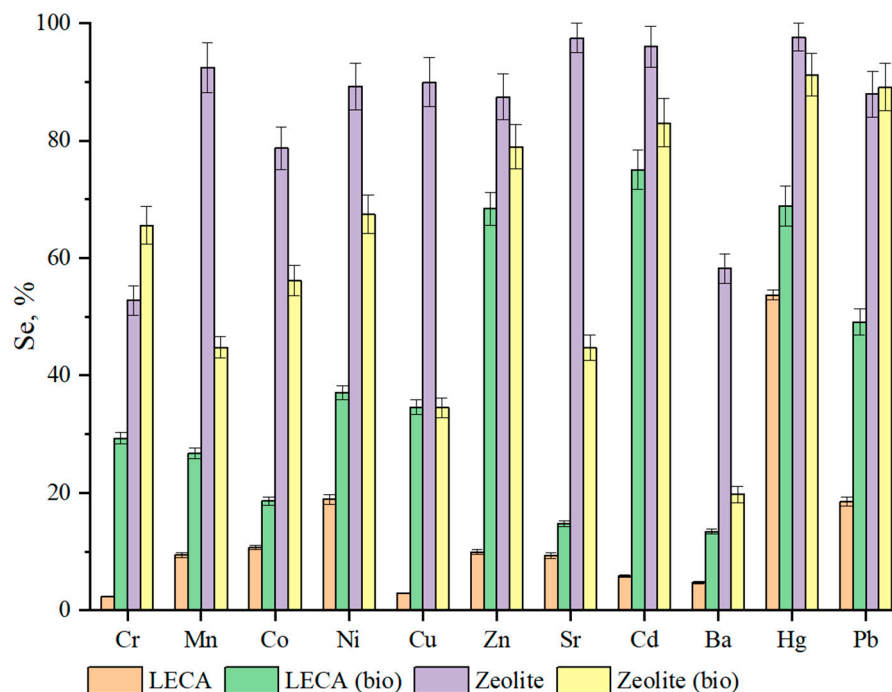
The area covered by cells (according to nucleic acid staining) on LECA was on average two times greater than that on zeolite (Table 3, which also contains data on the formation of biofilms in the biomineralization experiment). A similar trend was observed with the total covered area, in the case of zeolite, it was  $53 \pm 2.6\%$  and for LECA,  $84 \pm 4.1\%$ . The high biofouling of LECA is primarily due to its porous structure and larger surface area compared to zeolite.

**Table 3.** Topological parameters of biofilm on analyzed materials (after 20 days of growth) studied by confocal scanning laser microscopy.

Sample	Nucleic Acid, %	Polysaccharides, %	Total Area of Fouling, %
Zeolite–bio	5 ± 0.2	54 ± 2.6	59 ± 2.9
LECA–bio	14 ± 0.7	75 ± 3.8	89 ± 4.3
Zeolite–biomineralization	8 ± 0.4	45 ± 2.2	53 ± 2.6
LECA–biomineralization	13 ± 0.6	71 ± 3.6	84 ± 4.1

### 3.2. Metal Immobilization on Materials before and after Biofouling (Sorption Experiment)

The results of metal accumulation on raw and biofilm-coated materials are presented in Figure 2. The efficiency of metal sorption on LECA did not exceed 20%, with the exception of mercury, when the sorption efficiency was slightly above 50%. Sorption efficiency on zeolite was significantly higher. Thus, for cadmium, strontium, mercury, and manganese, it was higher than 90%, and for nickel, zinc, copper, and lead, it was in the range of 80–90%. Formation of biofilm on the analyzed materials had a multidimensional effect on the efficiency of sorption. For LECA, the efficiency of all metals' immobilization increased. The highest efficiency (60–80%) was observed for chromium, zinc, cadmium, and copper. For nickel, cobalt, strontium, and barium, the increase in the efficiency of immobilization was less pronounced. In the case of zeolite, the formation of biofilm resulted in the decrease in manganese, cobalt, nickel, copper, zinc, strontium, cadmium and barium immobilization. Moreover, for cobalt, copper, strontium and barium, the decrease in the sorption efficiency was significant (20–50%). For lead and mercury, the efficiency of immobilization was almost unaffected by the biofilm. Thus, the formation of biofilms on materials with high immobilization characteristics inhibits metal accumulation.

**Figure 2.** Metal immobilization on untreated and biofilm-coated materials.

### 3.3. Metal Immobilization on Materials during Biofouling (Bioaccumulation and Biomineralization Experiment)

The values of the efficiency of metal immobilization on the studied materials during biomass growth with and without the addition of the excess of phosphates in the medium

are presented in Table 4. Metal immobilization on materials, particularly for LECA, increased in the biomineralization experiments. Immobilization on LECA was higher than on zeolite, which can be attributed to the greater surface biofouling. The addition of phosphates contributed to the significant increase in strontium and barium immobilization and resulted in 100% immobilization of mercury.

**Table 4.** Efficiency (%) of metal immobilization on materials in biomineralization experiments with phosphates (bmp) and without phosphates (bm).

Metal	LECA (bio)	LECA (bm)	LECA (bmp)	Zeolite (bio)	Zeolite (bm)	Zeolite (bmp)
Cr	29.3 ± 1.0	97.5 ± 4.4	98.7 ± 4.3	65.5 ± 1.6	90.7 ± 4.0	91.5 ± 3.9
Mn	26.7 ± 1.0	98.7 ± 4.2	99.4 ± 4.5	44.8 ± 0.9	89.4 ± 3.7	90.8 ± 3.7
Co	18.6 ± 0.8	99.1 ± 4.5	98.1 ± 4.3	56.1 ± 1.9	82.3 ± 3.9	84.7 ± 2.9
Ni	37.1 ± 1.7	99.6 ± 4.5	99.5 ± 4.4	67.4 ± 2.0	82.32.6	99.5 ± 3.9
Cu	34.6 ± 1.4	92.5 ± 4.0	89.1 ± 3.0	34.5 ± 0.8	85.4 ± 2.4	88.1 ± 2.6
Zn	68.4 ± 3.4	98.9 ± 4.4	99.8 ± 4.7	78.9 ± 3.6	92.1 ± 4.0	90.4 ± 3.7
Sr	14.7 ± 0.7	31.2 ± 1.2	100 ± 5.0	44.7 ± 1.2	57.9 ± 1.9	100 ± 4.5
Cd	75 ± 3.0	98.1 ± 4.7	99.2 ± 4.3	83 ± 3.0	98.4 ± 3.8	99.1 ± 4.4
Ba	13.4 ± 0.3	16.2 ± 0.7	89.7 ± 3.8	19.7 ± 0.7	31.2 ± 1.5	98.5 ± 4.2
Hg	68.9 ± 2.5	100 ± 4.4	100 ± 4.5	91.2 ± 2.6	100 ± 4.8	100 ± 4.5
Pb	49.1 ± 1.8	97.9 ± 4.2	98.6 ± 3.9	89.1 ± 2.4	99.8 ± 4.8	99.3 ± 4.3

### 3.4. Evaluation of the Binding Strength of Immobilized Forms of Metals on Analyzed Materials

Table 5 report the data related to the efficiency of metal desorption using groundwater as a desorbing agent (2 h of mixing). According to the results, the strength of metal binding on zeolite was higher despite its lower fouling. In the experiment with LECA coated with biofilm, the highest efficiency of desorption was obtained for cobalt, chromium, copper, barium, and manganese, while for cadmium and zinc, it was very low. On zeolite coated with biofilms, the maximum desorption was observed for chromium and the minimum for cadmium. Thus, in sorption experiments, the majority of metals was not strongly immobilized on organic microbial biofilms.

**Table 5.** Efficiency of metal desorption from the LECA and zeolite using groundwater as a desorbing agent.

Metal	LECA (bio)	LECA (bm)	LECA (bmp)	Zeolite (bio)	Zeolite (bm)	Zeolite (bmp)
Cr	64.9 ± 2.9	2.2 ± 0.1	2.11 ± 0.01	41.9 ± 2.1	2.1 ± 0.01	1.7 ± 0.03
Mn	72.8 ± 3.5	1.3 ± 0.07	2.11 ± 0.01	32.3 ± 1.5	1.5 ± 0.01	1.9 ± 0.03
Co	81.6 ± 3.9	3.9 ± 0.09	4.1 ± 0.1	30.4 ± 1.4	3.1 ± 0.02	2.9 ± 0.4
Ni	49.4 ± 2.5	1.1 ± 0.03	1.8 ± 0.01	39.4 ± 1.9	0.9 ± 0.01	1.3 ± 0.01
Cu	54.3 ± 2.8	1.5 ± 0.05	1.71 ± 0.01	39.8 ± 1.7	1.9 ± 0.2	1.8 ± 0.03
Zn	43.4 ± 2.1	1.2 ± 0.06	0.9 ± 0.003	27.4 ± 1.2	3.9 ± 0.1	1.5 ± 0.03
Sr	52.9 ± 2.7	34.1 ± 1.4	1.91 ± 0.03	38.9 ± 1.7	28.3 ± 0.08	0.9 ± 0.02
Cd	43.6 ± 2.0	1.6 ± 0.05	1.5 ± 0.02	17.4 ± 0.8	1.3 ± 0.01	1.7 ± 0.01
Ba	77.7 ± 3.1	42.4 ± 2.1	2.11 ± 0.5	29.2 ± 1.0	20.1 ± 1.0	1.1 ± 0.02
Hg	12.8 ± 0.6	4.5 ± 0.0	3.1 ± 0.7	5.8 ± 0.01	1.1 ± 0.05	0.3 ± 0.001
Pb	49.2 ± 2.2	1.5 ± 0.5	0.34 ± 0.01	23.7 ± 1.2	1.1 ± 0.05	0.84 ± 0.02

The metal binding strength on both materials increased significantly during the biomineralization experiment. The highest efficiency of desorption for both materials was observed for Ba and Sr, and for other elements, it was less than 5%. At the addition of phosphates, the efficiency of elements desorption on LECA was less than 5% and on zeolite less than 3%.

#### 4. Discussion

The formation of biofilm on the studied materials occurred differently. The adhesion of biofilms on LECA was strengthened due to the more developed surface macrostructure and high roughness. However, since mesopores are inaccessible for microorganisms, the zeolite surface was not affected by biofouling. As a result, it can be assumed that biofouling and biofilm formation will influence metal immobilization only on LECA. Metal binding on zeolite can be influenced by biofilms as well as by the material's surface. The experiments revealed that the surfaces of materials, biofilms, and mineral phases formed during microorganism growth and contributed to metal immobilization. Furthermore, biomineralization was mainly responsible for metal immobilization. The mechanisms of metal fixation by microbial biofilms have been thoroughly investigated. They include physical and physicochemical adsorption, such as ion exchange or formation of complexes on biofilm sorption centers [34].

##### 4.1. The Role of Biofouling in Metals Immobilization

It is known that bacterial biofilms consist of a matrix with up to 90–95% polysaccharides based on  $\beta$ -glucuronic acid. The sorption sites of biofilms include hydroxyl (alcohols, carbohydrates), carboxyl (fatty acids, proteins, organic acid residues), amino groups (proteins and nucleic acids), esters (lipids), sulfhydryl groups (cysteine residues, proteins), aldehyde groups (aldehydes and polysaccharides), internal carbonyl groups (ketones and polysaccharides), and phosphate groups [35].

IR spectra recorded before and after the biofouling processes confirmed the materials' biogenic fouling. The spectrum of LECA after biofilm formation differed significantly from the spectrum of the raw material. Aluminosilicate-like bands were observed prior to biofilm formation: 1035, 799, and 775  $\text{cm}^{-1}$ . Two maxima, 993 and 918  $\text{cm}^{-1}$ , which are indicative of the stretching vibrations of the C-O and C-C groups, were identified on the band in the range of 1200–900  $\text{cm}^{-1}$  after biofouling (Figure 3a). The spectrum of the zeolite sample showed the appearance of  $\nu(\text{OH})$  stretching vibrations in the range of 3600–3300  $\text{cm}^{-1}$ , as well as the appearance of a band at 1414  $\text{cm}^{-1}$ , which can be attributed to the  $\delta(\text{COH})$  vibration. In addition, the spectrum of the bio-treated zeolite contained water vibration bands:  $\nu(\text{H}_2\text{O}) = 3528, 3381 \text{ cm}^{-1}$  and  $\delta(\text{H}_2\text{O}) = 1640 \text{ cm}^{-1}$ , which along with the hydroxy group, can be part of the polysaccharide matrix.

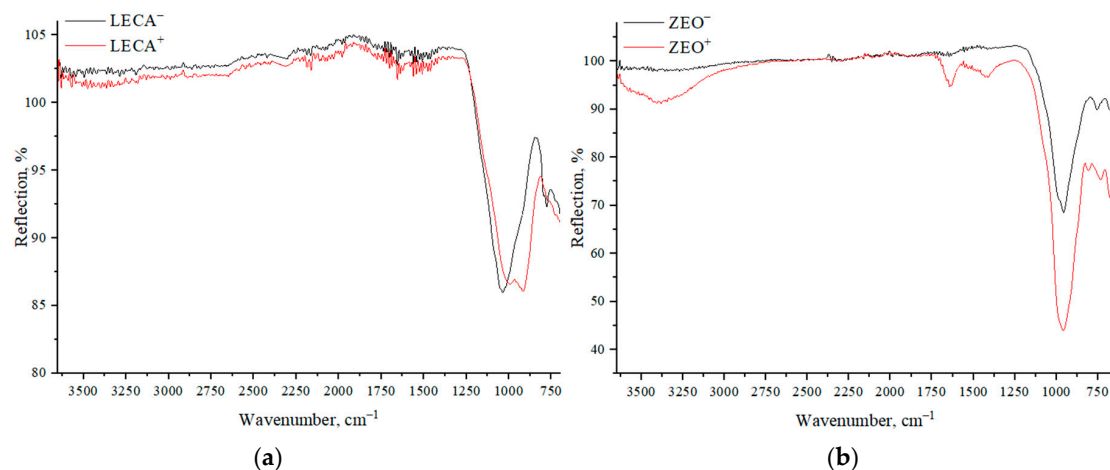


**Figure 3.** IR spectra of materials studied before and after biofouling: LECA (a) and zeolite (b).

According to the literature (Table A1), the most common complexing agents capable of chelating almost all metals used in the current study are carboxyl, hydroxyl, and thiol groups. Amino (and amide) groups are able to form compounds with Cr, Zn, Ni, Cu, Mn, Cd, Sr, and Hg. Phosphoryl groups have the lowest affinity for Mn, Co, and Sr. Although carbonyl groups can bind Cr, Ni, Cu, Hg, and Pb, their chelate formation is much less active.

Microbial biofilms can be considered as polyfunctional adsorbents for the majority of metals. At the same time the overlapping of the material's specific surface by the biological matrix can lead to the decrease in the material sorption capacity. This may explain the decrease in zeolite with biofilms sorption capacity toward Mn, Co, Ni, Cu, Sr, and Ba. It can be concluded that functional groups of zeolite play a dominant role in the binding of the mentioned metals.

#### 4.2. The Role of Biomineralization in Metal Immobilization

Previously, a microbial community capable of reducing iron, sulfur, and nitrogen compounds metabolically was discovered in water samples. In the present work, the effect of a single addition of organic matter on physico-chemical conditions was investigated experimentally (Figure 4). Significant shifts in the medium's redox potential toward the reduction region, as well as the reduction of nitrate ions, were observed up to day 30. Following the establishment of strongly reducing conditions, the concentration of sulfate ions decreased as a result of the sulfate reduction process, which led to sulfide reduction. The microbial processes were more active in the presence of LECA.

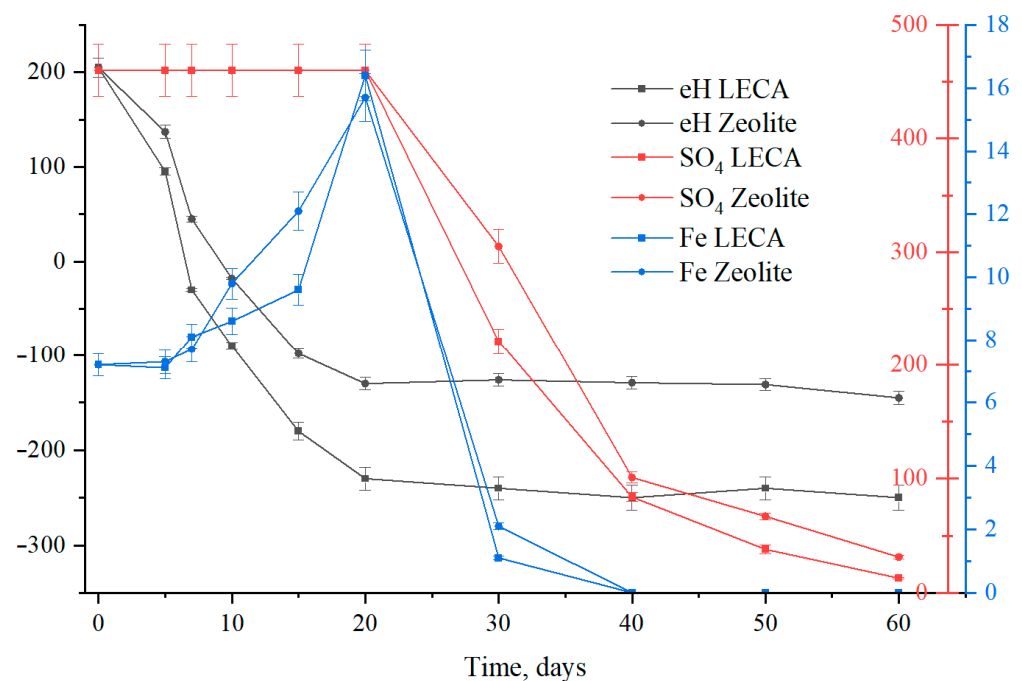


**Figure 4.** Kinetics of eH and Fe and  $\text{SO}_4^{2-}$  concentration change in solutions in biomineralization experiment.

Optional conditions for the solid mineral phases formation were determined according to calculation in PhreeqC code (the thermodynamic database *lnl.dat* was used) [33]. Sulfate-reductive conditions, a shift in the redox potential to the reduction side, and an increase in carbonate ion concentration are required. Carbonate mineral precipitation is primarily caused by anoxic microbial respiration. Sulfide and phosphates were formed in the system as a result of the sulfate reduction. Table 6 and Figure 5 show the results of the SI calculations of solid mineral phases under sulfate reduction conditions. For zinc phosphate (Hopeite,  $\text{Zn}_3(\text{PO}_4)_2 \cdot 4\text{H}_2\text{O}$ ), the SI was also greater than 0 (SI = 4.12).

**Table 6.** Thermodynamic modeling (PhreeqC 2.1 software with the llnl.dat) of mineral phases formation at saturation indices (SI) > 0.

Phase	Without Additions, pH 6.5	Sulfates Addition 500 mg, pH 8	Sulfates Addition 500 mg, Phosphates Addition, pH 8	Phosphates Addition, 500 mg	Formula
Carbonates					
Aragonite	−0.8	1.7	1.6	1.6	CaCO <sub>3</sub>
Calcite	−0.7	1.9	1.7	1.7	CaCO <sub>3</sub>
Cerussite	2.1	2.2	2.1	2.1	PbCO <sub>3</sub>
Dolomite	−0.7	4.6	4.2	4.2	CaMg(CO <sub>3</sub> ) <sub>2</sub>
Dolomite-dis	−2.3	3.0	2.5	2.5	CaMg(CO <sub>3</sub> ) <sub>2</sub>
Dolomite-ord	−0.7	4.6	4.2	4.2	CaMg(CO <sub>3</sub> ) <sub>2</sub>
Huntite	−7.5	3.3	2.3	2.3	CaMg <sub>3</sub> (CO <sub>3</sub> ) <sub>4</sub>
Hydrocerussite	3.5	3.7	3.4	3.4	Pb <sub>3</sub> (CO <sub>3</sub> ) <sub>2</sub> (OH) <sub>2</sub>
Monohydrocalcite	3.5	3.7	3.4	3.4	CaCO <sub>3</sub> :H <sub>2</sub> O
Magnesite	−1.6	1.0	0.7	0.7	MgCO <sub>3</sub>
Otavite	1.0	3.4	3.3	3.3	CdCO <sub>3</sub>
Rhodochrosite	−0.4	1.6	1.4	1.4	MnCO <sub>3</sub>
Siderite	−0.7	0.8	0.7	0.7	FeCO <sub>3</sub>
Smithsonite	−1.2	1.1	0.5	0.5	ZnCO <sub>3</sub>
Strontianite	−0.3	2.4	2.4	2.4	SrCO <sub>3</sub>
ZnCO <sub>3</sub> :H <sub>2</sub> O	−0.6	1.7	1.1	1.1	ZnCO <sub>3</sub> :H <sub>2</sub> O
Sulfides					
Alabandite	−1.6	0.9	0.6	0.7	MnS
Bornite	84.1	96.5	96.4	90.8	Cu <sub>5</sub> FeS <sub>4</sub>
Cattierite	9.2	13.3	13.3	12.4	CoS <sub>2</sub>
CdS	14.4	17.3	17.2	15.8	CdS
Chalcocite	30.8	34.2	34.2	32.8	Cu <sub>2</sub> S
Chalcopyrite	22.1	27.7	27.6	24.8	CuFeS <sub>2</sub>
CoS	3.8	4.3	4.3	4.8	CoS
Covellite	14.2	17.7	17.7	16.3	CuS
Galena	13.0	13.6	13.4	12.1	PbS
Metacinnabar	18.8	22.2	22.2	20.8	HgS
Millerite	6.3	9.6	9.6	8.2	NiS
Pyrite	6.7	12.4	12.3	9.5	FeS <sub>2</sub>
Pyrrhotite	1.6	3.7	3.5	2.1	FeS
Troilite	1.7	3.8	3.6	2.3	FeS
Vaesite	9.1	16.1	16.0	13.2	NiS <sub>2</sub>
Wurtzite	7.4	10.3	9.76	8.3	ZnS
Phosphates					
Hopeite			4.67	4.6	Zn <sub>3</sub> (PO <sub>4</sub> ) <sub>2</sub> :4H <sub>2</sub> O
Pb <sub>4</sub> O(PO <sub>4</sub> ) <sub>2</sub>			6.7	6.7	Pb <sub>4</sub> O(PO <sub>4</sub> ) <sub>2</sub>
PbHPO <sub>4</sub>			5.0	5.0	Pb <sub>4</sub> O(PO <sub>4</sub> ) <sub>2</sub>

Table 6. Cont.

Phase	Without Additions, pH 6.5	Sulfates Addition 500 mg, pH 8	Sulfates Addition 500 mg, Phosphates Addition, pH 8	Phosphates Addition, 500 mg	Formula
Oxyhydroxide					
Delafossite	4.9	9.4	9.3	9.3	CuFeO <sub>2</sub>

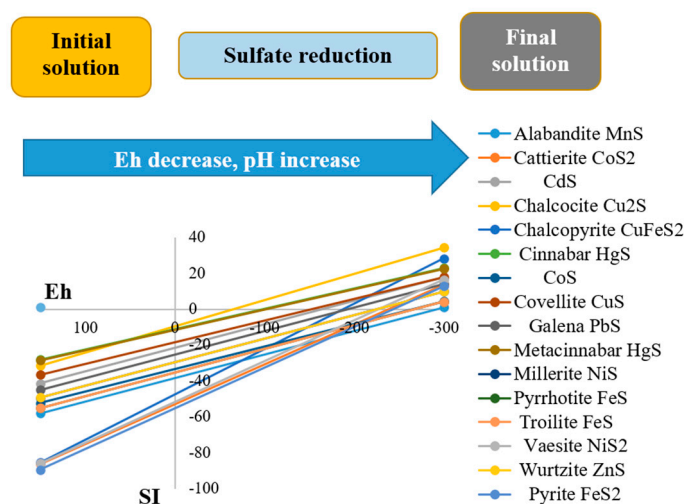


Figure 5. The results of solid mineral phases saturation index (SI) calculation under sulfate reduction conditions.

As a result of biogenic mineralization, according to BTC llnl.dat, the formation of the following metal phases was predicted: Mn in the form of MnCO<sub>3</sub> (Rhodochrosite) and in the form of MnS phases (Akabandite), Co as CoS<sub>2</sub> (Catterite), Cd as CdCO<sub>3</sub> (Otavite) and CdS, Cu as Cu<sub>2</sub>S (Chalcocite) and CuS (Covellite), Hg as HgS (Cinnabar), Ni as NiS (Mullerite) and NiS<sub>2</sub> (Vaesite), Zn as ZnCO<sub>3</sub> (Smithsonite) ZnS (Wurtzite), Pb in the form of Pb<sub>3</sub>(CO<sub>3</sub>)<sub>2</sub>(OH)<sub>2</sub> (Hydrocerussite) and PbCO<sub>3</sub> (Cerussite), as well as PbS (Galena), Fe in the form of FeCO<sub>3</sub> (Siderite) and various sulfide phases such as FeS<sub>2</sub> (Pyrite) and FeS (Troilite, Pirrhotite). The addition of phosphates, as well as the production of biogenic carbonate during decomposition of organic carbon, led to a significant decrease in the desorption of strontium and barium, while for other metals, the effect was less pronounced. This can be explained by the formation of calcium phosphate and biogenic calcite (the SI for monohydrocalcite was 0.42, for aragonite > 1, calcite > 1.2, and dolomite > 4), which with high probability, participated in the coprecipitation of strontium (including strontianite) and barium. The addition of phosphates could also lead to the formation of zinc phosphates of the Zn<sub>3</sub>(PO<sub>4</sub>)<sub>2</sub>:4H<sub>2</sub>O (Hopeite) type.

Iron phases under reducing conditions are the most valuable in the process of biogenic minerals formation. Although the formation of iron oxyhydroxides +3 was not anticipated, sulfide phases were predicted to form because of the highly reducing environment. The elemental maps (S, Fe) acquired using electron microscopy provided further evidence (Figure 6). The accumulation of sulfur and iron phases on LECA (L) and zeolite (Z) after microbial transformation (2) was observed. No substantial iron sulfide crystals were discovered by scanning electron microscopy since the experiment's time period was insufficient for their formation. The observed sulfide–iron formations were most likely associated with a microbial biofilm.

It is known that ferriferous phases (siderite, pyrite, and other iron sulfides) are active sorbents of metals. The resulting sulfide reacts with chalcophile metals [36] such as copper, iron and zinc [37–39]. In a study by Jong et al. [40], it was found that biogenic iron sulfide is a highly effective adsorbent for a wide range of metals and non-metals, including Pb(II),

Cu(II), Cd(II), Zn(II), Ni(II), Fe(II), and As(V). In addition to sorption, the formation of sulfide phases can lead to reduction and stabilization of the reduced phases of metals with varying degrees of oxidation, forming a reductive barrier on the material's surface.

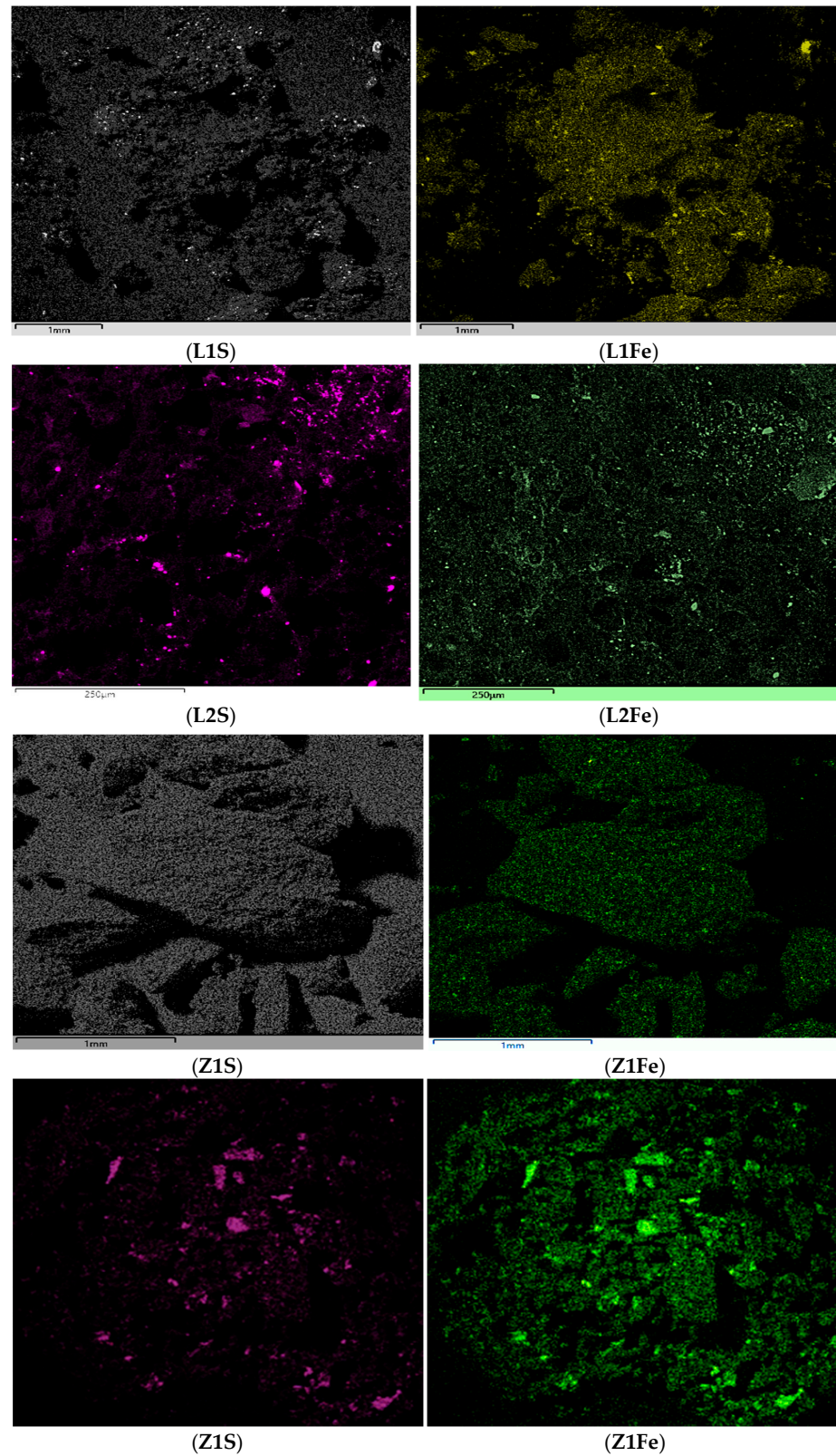


**Figure 6.** Microphotographs of the analyzed samples. Color mapping: purple for sulfur; yellow-green for iron.

## 5. Conclusions

The parameters of Cr, Mn, Co, Ni, Cu, Zn, Sr, Cd, Ba, Hg, and Pb immobilization on LECA and zeolite were established taking as an example the permeable biogeochemical barrier near the Siberian Chemical Plant multicomponent waste storage. The geochemical modeling approach predicted the formation of solid mineral phases of iron sulfides and other metals.

It has been established that microbial biofouling does not always promote metal immobilization on the mineral base of the barrier. Mesoporous materials with a high initial sorption capacity were affected by biofilm fouling, which reduced their sorption efficiency. However, biofouling had a beneficial effect on materials with a high surface area of macropores and a characteristically low capacity of metal sorption, significantly increasing their sorption capacity.

The non-uniformity of biofouling on zeolite and LECA demonstrated in this study suggested the feasibility of developing a permeable barrier for the purification of contaminated groundwater with specific functionality. The first component of the barrier can be zeolite, which is less susceptible to fouling and effectively immobilizes metals. LECA can be used as the second part of the barrier to remove metals, nitrates, and sulfates. It was discovered that the biomineralization process on LECA effectively retained metals in sulfide and phosphate forms. For metals of the non-chalcogen group, immobilization is possible with the addition of phosphates. The formation of biogenic iron sulfide precipitate during expanded clay loading is crucial, as it provides a sorption–precipitation phase for the immobilization of the majority of metals.

**Author Contributions:** Conceptualization, Investigation, Writing—original draft, A.S.; Formal analysis, Investigation, Writing—original draft, N.P.; Formal analysis, Investigation, L.D.; Investigation, N.Y.; Formal analysis K.B.; Investigation D.S.; Investigation G.A.; Investigation, Writing—original draft I.Z. All authors have read and agreed to the published version of the manuscript.

**Funding:** This work was supported by state assignments from The Ministry of Science and Higher Education of the Russian Federation (#AAAA-A16-11611091001) and was performed using the equipment of the Core Facilities Center of IPCE RAS (CKP FMI IPCE RAS).

**Institutional Review Board Statement:** Not applicable.

**Informed Consent Statement:** Not applicable.

**Data Availability Statement:** Not applicable.

**Conflicts of Interest:** The authors declare no conflict of interest. The authors declare that they have no known competing financial interests or personal relationships that could have appeared to influence the work reported in this paper.

## Appendix A

**Table A1.** The role of organic groups in metal immobilization according to literature data.

	Carboxyl	Carbonyl	Hydroxyl	Amino	Phosphoryl	Thiol (SH)
Cr	[41,42]	[43]	[44,45]	[44]	[44]	[41,45]
Mn	[46]	-	[46,47]	[46]	-	[46]
Co	[48,49]	[48]	[49,50]	[48]	-	[51]
Ni	[52,53]	[52,53]	[53,54]	[53]		-
Cu	[53,55,56]	[53,57]	[57]	[57]	[53,55,57]	[55]
Zn	[58–60]	-	[58]	[58]	[58,59]	[51,58,61,62]
Sr	[63]	-		[64]	-	[63]
Cd	[65–67]	-	[53,57]	[65,67]	[41]	[46]
Ba	[63]	-	-	-	[68]	[63]
Hg	[69–71]	[69]	[70,71]	[70,71]	[71]	[62,72–74]
Pb	[53,75]	[53]	[76,77]	-	[53,75–78]	[62,72–74]

## References

1. Safonov, A.V.; Boguslavsky, A.E.; Boldyrev, K.A.; Gaskova, O.L.; Naimushina, O.S.; Popova, N.M. Geochemical Modeling of the Uranium Behavior in Groundwater near the Sludge Storages during Bioremediation. *Geochem. Int.* **2021**, *59*, 56–65. [[CrossRef](#)]
2. Boguslavskii, A.E.; Gas'kova, O.L.; Shemelina, O.V. Geochemical Model of the Environmental Impact of Low-Level Radioactive Sludge Repositories in the Course of Their Decommissioning. *Radiochemistry* **2016**, *58*, 323–328. [[CrossRef](#)]
3. Safonov, A.V.; Boguslavsky, A.E.; Gaskova, O.L.; Boldyrev, K.A.; Shvartseva, O.S.; Khvashchevskaya, A.A.; Popova, N.M. Biogeochemical Modelling of Uranium Immobilization and Aquifer Remediation Strategies near Nccp Sludge Storage Facilities. *Appl. Sci.* **2021**, *11*, 2875. [[CrossRef](#)]
4. Conca, J.; Strietelmeier, E.; Lu, N.; Ware, S.D.; Taylor, T.P.; Kaszuba, J.; Wright, J. Treatability Study of Reactive Materials to Remediate Groundwater Contaminated with Radionuclides, Metals, and Nitrates in a Four-Component Permeable Reactive Barrier. In *Handbook of Groundwater Remediation Using Permeable Reactive Barriers*; Elsevier: Amsterdam, The Netherlands, 2003; pp. 221–252.
5. Benner, S.G.; Blowes, D.W.; Gould, W.D.; Herbert, R.B.; Ptacek, C.J. Geochemistry of a Permeable Reactive Barrier for Metals and Acid Mine Drainage. *Environ. Sci. Technol.* **1999**, *33*, 2793–2799. [[CrossRef](#)]
6. Ludwig, R.D.; McGregor, R.G.; Blowes; Benner, S.G.; Mountjoy, K. A Permeable Reactive Barrier for Treatment of Heavy Metals. *Ground Water* **2002**, *40*, 59–66. [[CrossRef](#)]
7. Thiruvengkatachari, R.; Vigneswaran, S.; Naidu, R. Permeable Reactive Barrier for Groundwater Remediation. *J. Ind. Eng. Chem.* **2008**, *14*, 145–156. [[CrossRef](#)]
8. Vignola, R.; Bagatin, R.; De Folly D'Auris, A.; Flego, C.; Nalli, M.; Ghisletti, D.; Millini, R.; Sisto, R. Zeolites in a Permeable Reactive Barrier (PRB): One Year of Field Experience in a Refinery Groundwater-Part 1: The Performances. *Chem. Eng. J.* **2011**, *178*, 204–209. [[CrossRef](#)]
9. Faisal, A.A.H.; Hmood, Z.A. Groundwater Protection from Cadmium Contamination by Zeolite Permeable Reactive Barrier. *Desalination Water Treat* **2015**, *53*, 1377–1386. [[CrossRef](#)]
10. Rocha, L.C.C.; Zuquette, L.V. Evaluation of Zeolite as a Potential Reactive Medium in a Permeable Reactive Barrier (PRB): Batch and Column Studies. *Geosciences* **2020**, *10*, 59. [[CrossRef](#)]
11. Skinner, S.J.W.; Schutte, C.F. The Feasibility of a Permeable Reactive Barrier to Treat Acidic Sulphate- and Nitrate-Contaminated Groundwater. *Water SA* **2006**, *32*, 129–135. [[CrossRef](#)]
12. Fuller, C.C.; Bargar, J.R.; Davis, J.A. Molecular-Scale Characterization of Uranium Sorption by Bone Apatite Materials for a Permeable Reactive Barrier Demonstration. *Environ. Sci. Technol.* **2003**, *37*, 4642–4649. [[CrossRef](#)] [[PubMed](#)]
13. Holmes, R.R.; Hart, M.L.; Kevern, J.T. Reuse of Drinking Water Treatment Waste for Remediation of Heavy Metal Contaminated Groundwater. *Groundw. Monit. Remediat.* **2019**, *39*, 69–79. [[CrossRef](#)]
14. Taha, G.M. Utilization of Low-Cost Waste Material Bagasse Fly Ash in Removing of  $\text{Cu}^{2+}$ ,  $\text{Ni}^{2+}$ ,  $\text{Zn}^{2+}$ , and  $\text{Cr}^{3+}$  from Industrial Waste Water. *Groundw. Monit. Remediat.* **2006**, *26*, 137–141. [[CrossRef](#)]
15. Thakur, A.K.; Vithanage, M.; Das, D.B.; Kumar, M. A Review on Design, Material Selection, Mechanism, and Modelling of Permeable Reactive Barrier for Community-Scale Groundwater Treatment. *Environ. Technol. Innov.* **2020**, *19*, 100917. [[CrossRef](#)]
16. Cantrell, K.J.; Kaplan, D.I.; Wietsma, T.W. Zero-Valent Iron for the in Situ Remediation of Selected Metals in Groundwater. *J. Hazard. Mater.* **1995**, *42*, 201–212. [[CrossRef](#)]
17. Gu, B.; Liang, L.; Dickey, M.J.; Yin, X.; Dai, S. Reductive Precipitation of Uranium(VI) by Zero-Valent Iron. *Environ. Sci. Technol.* **1998**, *32*, 3366–3373. [[CrossRef](#)]
18. Gibert, O.; Assal, A.; Devlin, H.; Elliot, T.; Kalin, R.M. Performance of a Field-Scale Biological Permeable Reactive Barrier for in-Situ Remediation of Nitrate-Contaminated Groundwater. *Sci. Total Environ.* **2019**, *659*, 211–220. [[CrossRef](#)]
19. Borch, T.; Kretzschmar, R.; Kappler, A.; Van Cappellen, P.; Ginder-Vogel, M.; Voegelin, A.; Campbell, K. Biogeochemical Redox Processes and their Impact on Contaminant Dynamics. *Environ. Sci. Technol.* **2010**, *44*, 15–23. [[CrossRef](#)]
20. Silva, G.; Pennafirme, S.; Lopes, R.; Lima, I.; Crapez, M. Imaging Techniques for Monitoring Bacterial Biofilms in Environmental Samples—An Important Tool for Bioremediation Studies. *BAOJ Microbiol.* **2017**, *3*, 1–15.
21. Zinicovscaia, I.; Yushin, N.; Grozdov, D.; Abdusamadzoda, D.; Safonov, A.; Rodlovskaya, E. Zinc-Containing Effluent Treatment Using *Shewanella Xiamenensis* Biofilm Formed on Zeolite. *Materials* **2021**, *14*, 1760. [[CrossRef](#)]
22. Zinicovscaia, I.; Safonov, A.; Boldyrev, K.; Gundorina, S.; Yushin, N.; Petuhov, O.; Popova, N. Selective Metal Removal from Chromium-Containing Synthetic Effluents Using *Shewanella Xiamenensis* Biofilm Supported on Zeolite. *Environ. Sci. Pollut. Res.* **2020**, *27*, 10495–10505. [[CrossRef](#)] [[PubMed](#)]
23. Zinicovscaia, I.; Yushin, N.; Grozdov, D.; Vergel, K.; Popova, N.; Artemiev, G.; Safonov, A. Metal Removal from Nickel-Containing Effluents Using Mineral–Organic Hybrid Adsorbent. *Materials* **2020**, *13*, 4462. [[CrossRef](#)] [[PubMed](#)]
24. Zinicovscaia, I.; Yushin, N.; Grozdov, D.; Safonov, A.; Ostovnaya, T.; Boldyrev, K.; Kryuchkov, D.; Popova, N. Bio-Zeolite Use for Metal Removal from Copper-Containing Synthetic Effluents. *J. Environ. Health Sci. Eng.* **2021**, *19*, 1383–1398. [[CrossRef](#)] [[PubMed](#)]
25. Kumar, N.; Chaurand, P.; Rose, J.; Diels, L.; Bastiaens, L. Synergistic effects of sulfate reducing bacteria and zero-valent iron on zinc removal and stability in aquifer sediment. *Chem. Eng.* **2015**, *260*, 83–89. [[CrossRef](#)]
26. Upadhyay, S.; Sinha, A. Role of microorganisms in permeable reactive bio-barriers (PRBBs) for environmental clean-up: A review. *Global NEST J.* **2018**, *20*, 269–280.

27. He, Y.T.; Wilson, J.T.; Wilkin, R.T. Transformation of Reactive Iron Minerals in a Permeable Reactive Barrier (Biowall) Used to Treat TCE in Groundwater. *Environ. Sci. Technol.* **2008**, *42*, 6690–6696. [[CrossRef](#)] [[PubMed](#)]
28. Safonov, A.V.; Andryushchenko, N.D.; Ivanov, P.V.; Boldyrev, K.A.; Babich, T.L.; German, K.E.; Zakharova, E.V. Biogenic Factors of Radionuclide Immobilization on Sandy Rocks of Upper Aquifers. *Radiochemistry* **2019**, *61*, 99–108. [[CrossRef](#)]
29. Safonov, A.V.; Babich, T.L.; Sokolova, D.S.; Grouzdev, D.S.; Tourova, T.P.; Poltarau, A.B.; Zakharova, E.V.; Merkel, A.Y.; Novikov, A.P.; Nazina, T.N. Microbial Community and in Situ Bioremediation of Groundwater by Nitrate Removal in the Zone of a Radioactive Waste Surface Repository. *Front. Microbiol.* **2018**, *9*, 1985. [[CrossRef](#)]
30. Pavlov, S.S.; Dmitriev, A.Y.; Frontasyeva, M.V. Automation system for neutron activation analysis at the reactor IBR-2, Frank Laboratory of Neutron Physics, Joint Institute for Nuclear Research, Dubna, Russia. *JRNC* **2016**, *309*, 27–38. [[CrossRef](#)]
31. Bogachev, M.I.; Volkov, V.Y.; Markelov, O.A.; Trizna, E.Y.; Baydamshina, D.R.; Melnikov, V.; Murtazina, R.R.; Zelenikhin, P.V.; Sharafutdinov, I.S.; Kayumov, A.R. Fast and simple tool for the quantification of biofilm-embedded cells sub-populations from fluorescent microscopic images. *PLoS ONE* **2018**, *13*, e0193267. [[CrossRef](#)]
32. Trafny, E.A.; Lewandowski, R.; Zawistowska-Marciniak, I.; Stępińska, M. Use of MTT assay for determination of the biofilm formation capacity of microorganisms in metalworking fluids. *World J. Microbiol. Biotechnol.* **2013**, *29*, 1635–1643. [[CrossRef](#)] [[PubMed](#)]
33. Parkhurst, D. User's Guide to PHREEQC—A Computer Program for Speciation, Reaction-Path, Advective-Transport, and Inverse Geochemical Calculations. *US Geol. Surv. Water-Resour. Investig. Rep.* **1995**, *143*, 95–4227. [[CrossRef](#)]
34. Javanbakht, V.; Alavi, S.A.; Zilouei, H. Mechanisms of Heavy Metal Removal Using Microorganisms as Biosorbent. *Water Sci. Technol.* **2014**, *69*, 1775–1787. [[CrossRef](#)] [[PubMed](#)]
35. Sag, Y.; Kutsal, T. Recent Trends in the Biosorption of Heavy Metals: A Review. *Biotechnol. Bioprocess Eng.* **2001**, *6*, 376–385. [[CrossRef](#)]
36. Viggì, C.C.; Pagnanelli, F.; Toro, L. Sulphate Reduction Processes in Biological Permeable Reactive Barriers: Column Experimentation and Modeling. In *Chemical Engineering Transactions*; Italian Association of Chemical Engineering—AIDIC: Milan, Italy, 2011; Volume 24, pp. 1231–1236.
37. Marius, M.S.; James, P.A.B.; Bahaj, A.S.; Smallman, D.J. Influence of Iron Valency on the Magnetic Susceptibility of a Microbially Produced Iron Sulphide. In *Journal of Physics: Conference Series*; Institute of Physics Publishing: Bristol, UK, 2005; Volume 17, pp. 65–69.
38. Mokone, T.P.; van Hille, R.P.; Lewis, A.E. Metal Sulphides from Wastewater: Assessing the Impact of Supersaturation Control Strategies. *Water Res.* **2012**, *46*, 2088–2100. [[CrossRef](#)]
39. Martins, M.; Faleiro, M.L.; Barros, R.J.; Veríssimo, A.R.; Barreiros, M.A.; Costa, M.C. Characterization and Activity Studies of Highly Heavy Metal Resistant Sulphate-Reducing Bacteria to Be Used in Acid Mine Drainage Decontamination. *J. Hazard. Mater.* **2009**, *166*, 706–713. [[CrossRef](#)] [[PubMed](#)]
40. Jong, T.; Parry, D.L. Adsorption of Pb(II), Cu(II), Cd(II), Zn(II), Ni(II), Fe(II), and As(V) on Bacterially Produced Metal Sulfides. *J. Colloid Interface Sci.* **2004**, *275*, 61–71. [[CrossRef](#)]
41. Sobol, Z.; Schiestl, R.H. Intracellular and Extracellular Factors Influencing Cr(VI) and Cr(III) Genotoxicity. *Environ. Mol. Mutagen.* **2012**, *53*, 94–100. [[CrossRef](#)]
42. Li, S.; Zhou, Z.; Tie, Z.; Wang, B.; Ye, M.; Du, L.; Cui, R.; Liu, W.; Wan, C.; Liu, Q.; et al. Data-Informed Discovery of Hydrolytic Nanozymes. *Nat. Commun.* **2022**, *13*, 1–12. [[CrossRef](#)]
43. Jobby, R.; Jha, P.; Yadav, A.K.; Desai, N. Biosorption and Biotransformation of Hexavalent Chromium [Cr(VI)]: A Comprehensive Review. *Chemosphere* **2018**, *207*, 255–266. [[CrossRef](#)]
44. An, H.; Tian, T.; Wang, Z.; Jin, R.; Zhou, J. Role of Extracellular Polymeric Substances in the Immobilization of Hexavalent Chromium by *Shewanella Putrefaciens* CN32 Unsaturated Biofilms. *Sci. Total Environ.* **2022**, *810*, 151184. [[CrossRef](#)] [[PubMed](#)]
45. Viti, C.; Marchi, E.; Decorosi, F.; Giovannetti, L. Molecular Mechanisms of Cr(VI) Resistance in Bacteria and Fungi. *FEMS Microbiol. Rev.* **2014**, *38*, 633–659. [[CrossRef](#)] [[PubMed](#)]
46. Huang, H.; Zhao, Y.; Xu, Z.; Ding, Y.; Zhou, X.; Dong, M. A High Mn(II)-Tolerance Strain, *Bacillus Thuringiensis* HM7, Isolated from Manganese Ore and Its Biosorption Characteristics. *PeerJ* **2020**, *8*, e8589. [[CrossRef](#)] [[PubMed](#)]
47. Snyder, M.S. *Biological Control of Manganese in Water Supplies in the Presence of Humic Acids*; University of Kentucky: Lexington, KY, USA, 2013.
48. Fawzy, M.A.; Hifney, A.F.; Adam, M.S.; Al-Badaani, A.A. Biosorption of Cobalt and Its Effect on Growth and Metabolites of *Synechocystis Pevalekii* and *Scenedesmus Bernardii*: Isothermal Analysis. *Environ. Technol. Innov.* **2020**, *19*, 100953. [[CrossRef](#)]
49. Su, Y.; Sun, S.; Liu, Q.; Zhao, C.; Li, L.; Chen, S.; Chen, H.; Wang, Y.; Tang, F. Characterization of the Simultaneous Degradation of Pyrene and Removal of Cr(VI) by a Bacteria Consortium YH. *Sci. Total Environ.* **2022**, *853*, 158388. [[CrossRef](#)]
50. Waris, A.; Din, M.; Ali, A.; Afridi, S.; Baset, A.; Khan, A.U.; Ali, M. Green Fabrication of Co and Co<sub>3</sub>O<sub>4</sub> nanoparticles and Their Biomedical Applications: A Review. *Open Life Sci.* **2021**, *16*, 14–30. [[CrossRef](#)]
51. Dulay, H.; Tabares, M.; Kashefi, K.; Reguera, G. Cobalt Resistance via Detoxification and Mineralization in the Iron-Reducing Bacterium *Geobacter Sulfurreducens*. *Front. Microbiol.* **2020**, *11*, 600463. [[CrossRef](#)]
52. Levett, A.; Gleeson, S.A.; Kallmeyer, J. From Exploration to Remediation: A Microbial Perspective for Innovation in Mining. *Earth Sci. Rev.* **2021**, *216*, 103563. [[CrossRef](#)]

53. Haque, M.M.; Mosharaf, M.K.; Haque, M.A.; Tanvir, M.Z.H.; Alam, M.K. Biofilm Formation, Production of Matrix Compounds and Biosorption of Copper, Nickel and Lead by Different Bacterial Strains. *Front. Microbiol.* **2021**, *12*, 1385. [[CrossRef](#)]
54. Haider, A.; Ijaz, M.; Ali, S.; Haider, J.; Imran, M.; Majeed, H.; Shahzadi, I.; Ali, M.M.; Khan, J.A.; Ikram, M. Green Synthesized Phytochemically (Zingiber Officinale and Allium Sativum) Reduced Nickel Oxide Nanoparticles Confirmed Bactericidal and Catalytic Potential. *Nanoscale Res. Lett.* **2020**, *15*, 1–11. [[CrossRef](#)]
55. Lin, H.; Wang, C.; Zhao, H.; Chen, G.; Chen, X. A Subcellular Level Study of Copper Speciation Reveals the Synergistic Mechanism of Microbial Cells and EPS Involved in Copper Binding in Bacterial Biofilms. *Environ. Pollut.* **2020**, *263*, 114485. [[CrossRef](#)] [[PubMed](#)]
56. Fang, L.; Yang, S.; Huang, Q.; Xue, A.; Cai, P. Biosorption Mechanisms of Cu(II) by Extracellular Polymeric Substances from *Bacillus Subtilis*. *Chem. Geol.* **2014**, *386*, 143–151. [[CrossRef](#)]
57. Cheng, X.; Xu, W.; Wang, N.; Mu, Y.; Zhu, J.; Luo, J. Adsorption of Cu<sup>2+</sup> and Mechanism by Natural Biofilm. *Water Sci. Technol.* **2018**, *78*, 721–731. [[CrossRef](#)] [[PubMed](#)]
58. Thomas, S.A.; Mishra, B.; Myneni, S.C.B. High Energy Resolution-X-Ray Absorption Near Edge Structure Spectroscopy Reveals Zn Ligation in Whole Cell Bacteria. *J. Phys. Chem. Lett.* **2019**, *10*, 2585–2592. [[CrossRef](#)]
59. Li, C.C.; Wang, Y.J.; Du, H.; Cai, P.; Peijnenburg, W.J.G.M.; Zhou, D.M. Influence of Bacterial Extracellular Polymeric Substances on the Sorption of Zn on  $\gamma$ -Alumina: A Combination of FTIR and EXAFS Studies. *Environ. Pollut.* **2017**, *220*, 997–1004. [[CrossRef](#)]
60. Basak, G.; Lakshmi, V.; Chandran, P.; Das, N. Removal of Zn(II) from Electroplating Effluent Using Yeast Biofilm Formed on Gravels: Batch and Column Studies. *J. Environ. Health Sci. Eng.* **2014**, *12*, 8. [[CrossRef](#)]
61. Desmau, M.; Carboni, A.; Le Bars, M.; Doelsch, E.; Benedetti, M.F.; Auffan, M.; Levard, C.; Gelabert, A. How Microbial Biofilms Control the Environmental Fate of Engineered Nanoparticles? *Front. Environ. Sci.* **2020**, *8*, 82. [[CrossRef](#)]
62. Kumar, R.; Umar, A.; Kumar, G.; Nalwa, H.S. Antimicrobial Properties of ZnO Nanomaterials: A Review. *Ceram. Int.* **2017**, *43*, 3940–3961. [[CrossRef](#)]
63. Deng, N.; Stack, A.G.; Weber, J.; Cao, B.; De Yoreo, J.J.; Hu, Y. Organic–Mineral Interfacial Chemistry Drives Heterogeneous Nucleation of Sr-Rich (Bax, Sr<sup>1-x</sup>)SO<sub>4</sub> from Undersaturated Solution. *Proc. Natl. Acad. Sci. USA* **2019**, *116*, 13221–13226. [[CrossRef](#)]
64. Liu, M.; Dong, F.; Zhang, W.; Nie, X.; Wei, H.; Sun, S.; Zhong, X.; Liu, Y.; Wang, D. Contribution of Surface Functional Groups and Interface Interaction to Biosorption of Strontium Ions by *Saccharomyces Cerevisiae* under Culture Conditions. *RSC Adv.* **2017**, *7*, 50880–50888. [[CrossRef](#)]
65. Zhang, J.; Li, Q.; Zeng, Y.; Zhang, J.; Lu, G.; Dang, Z.; Guo, C. Bioaccumulation and Distribution of Cadmium by *Burkholderia Cepacia* GYP1 under Oligotrophic Condition and Mechanism Analysis at Proteome Level. *Ecotoxicol. Environ. Saf.* **2019**, *176*, 162–169. [[CrossRef](#)] [[PubMed](#)]
66. Boyanov, M.I.; Kelly, S.D.; Kemner, K.M.; Bunker, B.A.; Fein, J.B.; Fowle, D.A. Adsorption of Cadmium to *Bacillus Subtilis* Bacterial Cell Walls: A PH-Dependent X-Ray Absorption Fine Structure Spectroscopy Study. *Geochim. Cosmochim. Acta* **2003**, *67*, 3299–3311. [[CrossRef](#)]
67. Xu, S.; Xing, Y.; Liu, S.; Luo, X.; Chen, W.; Huang, Q. Co-Effect of Minerals and Cd(II) Promoted the Formation of Bacterial Biofilm and Consequently Enhanced the Sorption of Cd(II). *Environ. Pollut.* **2020**, *258*, 113774. [[CrossRef](#)]
68. Martinez-Ruiz, F.; Iroundi, F.; Paytan, A.; Guerra-Tschuschke, I.; Abad, M.D.M.; González-Muñoz, M.T. Barium Bioaccumulation by Bacterial Biofilms and Implications for Ba Cycling and Use of Ba Proxies. *Nat. Commun.* **2018**, *9*, 1–9. [[CrossRef](#)] [[PubMed](#)]
69. Bourdineaud, J.P.; Durn, G.; Režun, B.; Manceau, A.; Hrenović, J. The Chemical Species of Mercury Accumulated by *Pseudomonas Idrijaensis*, a Bacterium from a Rock of the Idrija Mercury Mine, Slovenia. *Chemosphere* **2020**, *248*, 126002. [[CrossRef](#)] [[PubMed](#)]
70. Fathollahi, A.; Coupe, S.J.; El-Sheikh, A.H.; Sañudo-Fontaneda, L.A. The Biosorption of Mercury by Permeable Pavement Biofilms in Stormwater Attenuation. *Sci. Total Environ.* **2020**, *741*, 140411. [[CrossRef](#)]
71. Dash, H.R.; Das, S. Interaction between Mercuric Chloride and Extracellular Polymers of Biofilm-Forming Mercury Resistant Marine Bacterium: *Bacillus Thuringiensis* PW-05. *RSC Adv.* **2016**, *6*, 109793–109802. [[CrossRef](#)]
72. Desmau, M.; Levard, C.; Vidal, V.; Ona-Nguema, G.; Charron, G.; Benedetti, M.F.; Gélabert, A. How Microbial Biofilms Impact the Interactions of Quantum Dots with Mineral Surfaces? *NanoImpact* **2020**, *19*, 100247. [[CrossRef](#)]
73. Yu, Q.; Szymanowski, J.; Myneni, S.C.B.; Fein, J.B. Characterization of Sulfhydryl Sites within Bacterial Cell Envelopes Using Selective Site-Blocking and Potentiometric Titrations. *Chem. Geol.* **2014**, *373*, 50–58. [[CrossRef](#)]
74. Mishra, B.; Shoenfelt, E.; Yu, Q.; Yee, N.; Fein, J.B.; Myneni, S.C.B. Stoichiometry of Mercury-Thiol Complexes on Bacterial Cell Envelopes. *Chem. Geol.* **2017**, *464*, 137–146. [[CrossRef](#)]
75. Templeton, A.S.; Trainor, T.P.; Spormann, A.M.; Newville, M.; Sutton, S.R.; Dohnalkova, A.; Gorby, Y.; Brown, G.E. Sorption versus Biomineralization of Pb(II) within *Burkholderia Cepacia* Biofilms. *Environ. Sci. Technol.* **2003**, *37*, 300–307. [[CrossRef](#)] [[PubMed](#)]
76. Sowmya, M.; Mohamed Hatha, A.A. Cadmium and Lead Tolerance Mechanisms in Bacteria and the Role of Halotolerant and Moderately Halophilic Bacteria in Their Remediation. In *Handbook of Metal-Microbe Interactions and Bioremediation*; CRC Press: Boca Raton, FL, USA, 2017; pp. 557–573. ISBN 9781315153353.

77. Kumari, S.; Mangwani, N.; Das, S. Interaction of Pb(II) and Biofilm Associated Extracellular Polymeric Substances of a Marine Bacterium *Pseudomonas Pseudoalcaligenes* NP103. *Spectrochim Acta A Mol. Biomol. Spectrosc.* **2017**, *173*, 655–665. [[CrossRef](#)] [[PubMed](#)]
78. Ngwenya, B.T.; Sutherland, I.W.; Kennedy, L. Comparison of the Acid-Base Behaviour and Metal Adsorption Characteristics of a Gram-Negative Bacterium with Other Strains. *Appl. Geochem.* **2003**, *18*, 527–538. [[CrossRef](#)]

**Disclaimer/Publisher's Note:** The statements, opinions and data contained in all publications are solely those of the individual author(s) and contributor(s) and not of MDPI and/or the editor(s). MDPI and/or the editor(s) disclaim responsibility for any injury to people or property resulting from any ideas, methods, instructions or products referred to in the content.